(Received 21 October 2025, Accepted 20 November 2025, Scheduled 19 December 2025)

Unbalance Vibration Compensation Control of Permanent Magnet Assisted Bearingless Synchronous Reluctance Motor Based on LMS Filter Algorithm Optimized by BPNN

Tianliang Du* and Huangqiu Zhu*

School of Electrical and Information Engineering, Jiangsu University, Zhenjiang 212013, China

ABSTRACT: To address the rotor vibration induced by rotor unbalance in a permanent magnet assisted bearingless synchronous reluctance motor (PMa-BSynRM), a feedforward compensation control method based on the Least Mean Squares (LMS) adaptive filtering algorithm, optimized by a Back Propagation Neural Network (BPNN), is proposed. Firstly, the operating principle of the PMa-BSynRM is introduced, and the mechanism of rotor unbalance vibration is analyzed. Secondly, a feedforward compensation controller is developed to extract the vibration signal and suppress rotor vibration. The BPNN is employed to adaptively adjust the LMS step size, thereby enhancing convergence speed, accuracy, and anti-interference capability. Furthermore, to overcome the inherent limitations of the BPNN, a hybrid optimization strategy that integrates particle swarm optimization (PSO) with an improved genetic algorithm (IGA) is adopted to optimize the initial weights and thresholds of the BPNN. Finally, a rotor unbalance vibration compensation control system for the PMa-BSynRM is established. Simulated and experimental results verify that the proposed control algorithm effectively reduces radial displacement and suppresses unbalanced vibration, while also exhibiting strong anti-interference performance and robustness.

1. INTRODUCTION

Bearingless motor is a novel type of electric motor that integrates the functions of active magnetic bearing (AMB) and motor. By inserting suspension force windings into the stator, it generates radial suspension force on the rotor, enabling stable suspension of the rotor. Through decoupled control, the torque and suspension forces of motor can be independently regulated. Compared with the active magnetic bearing, the bearingless motor reduces the axial length of the motor, lowers system costs, and enhances critical rotational speeds. The motor retains advantages of AMB — such as maintenance-free operation, long lifespan, and pollution-free transmission, while overcoming limitations like structural complexity and high costs [1].

Permanent Magnet Assisted Bearingless Synchronous Reluctance Motor (PMa-BSynRM) is a novel motor topology that integrates the technologies of Permanent Magnet Assisted Synchronous Reluctance Motor (PMa-SynRM) and bearingless motor. It achieves higher torque density and superior speed-regulation performance with fewer permanent magnets, while maintaining low cost and structural simplicity. This design is suitable for applications in industrial machine tools, aerospace, new energy vehicles, and life-science equipment [2].

In practical manufacturing, due to factors such as rotor material properties, machining accuracy, and assembly processes, inconsistency between the rotor's center of mass and geometric center is inevitable. During operation, the rotor produces an unbalanced centrifugal force whose amplitude increases proportionally with rotational speed, thereby inducing unbalance vibration. Consequently, effective unbalance rotor vibration compensation is essential for achieving stable suspension in the PMa-BSynRM. Existing unbalance vibration compensation approaches can be generally classified into two main categories.

One method is called inertial force minimum compensation [3], whose basic idea is to eliminate the speed equal frequency component in the output signal of the displacement sensor, so as to effectively reduce the response of the system to the unbalance disturbances, so that the rotor rotates around the inertial axis as far as possible, and reduce the unbalance force transmitted to the base.

Ref. [4] achieves adaptive automatic balancing control by obtaining unbalance Fourier coefficients through an iterative algorithm. In [5], a two-stage notch filter method is proposed to suppress synchronous vibration in magnetic levitation rotor systems across the full speed range. This approach adjusts the phase of the notch filter to ensure system stability throughout the entire operating speed range.

The other method is displacement minimum compensation. The principle is to increase the control current in the suspension force winding of the motor by analyzing the synchronous frequency component of the rotor vibration signal, make the rotor rotate around its geometric center as much as possible, improve the rotation accuracy of the rotor, so as to suppress the unbalance vibration [3].

Ref. [6] inserts a sensitivity adjustment matrix into the trap, which ensured the system stability in different rotational speed ranges. Ref. [7] adopts an LQG controller composed of an

* Corresponding authors: Tianliang Du (dutianliang0503@163.com); Huangqiu Zhu (zhuhuangqiu@ujs.edu.cn).

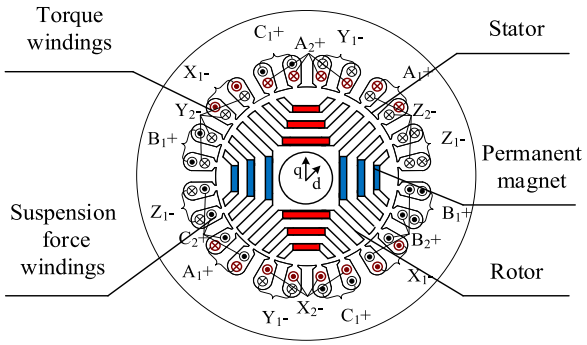

FIGURE 1. Basic structure of the PMa-BSynRM.

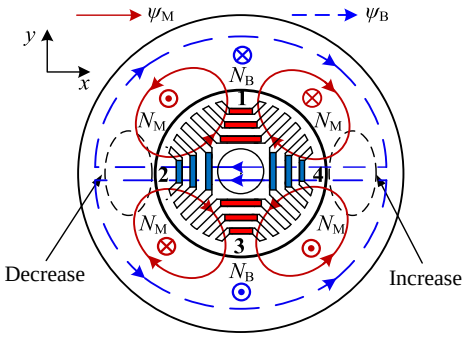

FIGURE 2. Principle of the suspension force generation.

extended Kalman filter and optimal state feedback regulator, which improves the rotor position accuracy and compensates for the vibration caused by the unbalance. In [8], a variable angle compensation algorithm is proposed, first, the vibration signal processing module calculates the vibration signal amplitude, then searches the unbalance coefficient to minimize the unbalanced vibration, and finally generates the compensation current to offset the unbalance vibration. In [9], a fuzzy gain adjustment mechanism is proposed to reduce the unbalance vibration of the maglev rotor system, and the unbalance force and unbalance displacement observer is designed. In [10], a variable step-size compensation method is proposed for unbalance vibration suppression in magnetic levitation rotor systems. By using the fundamental frequency vibration amplitude as an identification index, the literature dynamically adjusted the search step size based on real-time vibration signal amplitude. This approach achieves displacement vibration compensation through adaptive control current modulation, and the algorithm effectively suppresses displacement vibration during the rotor acceleration phase. However, when the rotor vibration approaches the set point, the small step size of the triangular search algorithm leads to increased search time. In [11], a recursive search-based unbalance compensation method is proposed for active magnetic bearing rotor systems. By recursively identifying the position of unbalance mass and adaptively adjusting compensation signals in real time, this approach effectively suppresses rotor vibration and improves rotational accuracy. Compared to traditional methods, it significantly reduces computational costs during variable-speed operation while exhibiting superior stability and convergence.

Most of the above methods rely on the extraction of unbalanced synchronous signals in the displacement signal. In addition, model-based control approaches have been explored. For instance, the method in [12] simultaneously estimates dynamic parameters and unbalance quantities based on rotor models, achieving satisfactory control performance. However, such approaches heavily depend on model accuracy, and constructing precise dynamic models poses significant challenges in practical applications. Consequently, adaptive filtering algorithms for synchronous unbalance signal extraction remain the most widely adopted solutions. The Least Mean Square (LMS) adaptive filtering algorithm is widely applied in rotor unbalance vibration compensation due to its simple structure and strong tracking capabilities [13]. However, conventional fixed-step LMS algorithms face inherent limitations in balancing convergence speed and precision, resulting in insufficient real-time performance and accuracy for practical requirements. A Versoria function-based variable step-size LMS adaptive filter is proposed in [14] to effectively compensate for rotor unbalance vibration, bringing the rotor closer to its geometric center and enhancing the application value of magnetic bearings in high-speed and high-precision scenarios. While the LMS algorithm exhibits strong convergence performance under Gaussian noise interference in practical applications, its convergence capability deteriorates significantly when being confronted with non-Gaussian noise characterized by pronounced impulsive characteristics [15].

An unbalance feed-forward compensation control method based on a new LMS adaptive filtering algorithm, using LMS adaptive filtering algorithm to extract the unbalance signal and adopt the displacement minimum principle, is proposed in this paper, while introducing a BP neural network (BPNN) to adjust the step factor which improve the convergence speed, accuracy and anti-interference ability of LMS algorithm. Moreover, considering that the BPNN itself has the disadvantage of easily falling into local optimal, which affects its convergence speed and accuracy, the initial weights and thresholds of the BPNN are optimized by combining particle swarm optimization (PSO) and an improved genetic algorithm (IGA). Finally, a rotor unbalance vibration compensation control system of PMa-BSynRM is established to verify the accuracy and feasibility of the proposed method through simulation and experiments.

2. OPERATION PRINCIPLE AND ROTOR VIBRATION MECHANISM OF THE PMA-BSYNRM

2.1. Operation Principle of the PMa-BSynRM

Figure 1 shows the basic structure diagram of the PMa-BSynRM, with the structure of 24 stator slots and double-layer winding, outer layer is suspension force winding using concentric winding structure, inner layer is torque winding using chain winding structure. The rotor adopts a three-layer magnetic barrier type rotor and inserts an appropriate amount of permanent magnet. The torque generation principle of PMa-BSynRM is the same as that of conventional convex pole motors based on the principle of minimum magnetic resistance.

Figure 2 is the schematic diagram of the suspension force generation, and the winding is equivalent; N_B is the suspension force winding; N_M is the torque winding; ψ_B is the suspension force winding magnetic chain; ψ_M is the torque winding magnetic chain. At the air gap 4 in the positive direction of the x axis, ψ_M and ψ_B are in the same direction, and the magnetic field is enhanced. At the air gap 2 in the negative direction of the x axis, ψ_M and ψ_B are in the opposite directions, and the magnetic field is weakened, resulting in a radial suspension force in the positive direction of the x axis. The amplitude and direction of the suspension force are controlled by changing the phase and magnitude of the suspension force current.

2.2. Mathematical Model of PMa-BSynRM

In the PMa-BSynRM model, the change of the rotor in radial displacement affects the magnetic chain of the suspension force and torque windings, and there is a coupling relationship between the windings current and magnetic chain, and the magnetic chain equation of PMa-BSynRM can be expressed as:

$$\begin{bmatrix} \psi_{Md} \\ \psi_{Mq} \\ \psi_{Bd} \\ \psi_{Bq} \end{bmatrix} = \begin{bmatrix} L_{Md} & 0 & M_d x_d & -M_d y_q \\ 0 & L_{Mq} & M_q y_q & M_q x_d \\ M_d x_d & M_q y_q & L_B & 0 \\ -M_d y_q & M_q x_d & 0 & L_B \end{bmatrix} \cdot \begin{bmatrix} i_{Md} \\ i_{Mq} - i_0 \\ i_{Bd} \\ i_{Bq} \end{bmatrix} \tag{1}$$

where ψ_{Md}, ψ_{Mq} are the d- and q-axis equivalent air gap flux linkages associated with the torque windings for the d- and q-axes; ψ_{Bd}, ψ_{Bq} are the corresponding equivalent air gap flux linkages related to the suspension force windings; L_{Md}, L_{Mq} are the self-inductances of the torque windings, along the d- and q-axes; L_B is the self-inductance of the suspension force windings; M_d, M_q are the suspension force constants, while x_d, y_q are the rotor radial displacement components for the d- and q-axes; i_{Md}, i_{Mq} are the equivalent control currents of the torque windings on the d- and q-axes, respectively; i_0 is the equivalent excitation current of the permanent magnet defined opposite to the direction of q-axis; i_{Bd}, i_{Bq} are the equivalent control currents of the suspension force windings for the d- and q-axes [16].

On the basic of the magnetic chain equation obtained from Equation (1), the deduced magnetic conergy equation for the PMa-BSynRM is:

$$\begin{aligned} W_m &= \frac{1}{2} \begin{bmatrix} i_{Md} & i_{Mq} - i_0 & i_{Bd} & i_{Bq} \end{bmatrix} \cdot \begin{bmatrix} \psi_{Md} & \psi_{Mq} & \psi_{Bd} & \psi_{Bq} \end{bmatrix}^T \\ &= \frac{1}{2} \left[L_{Md} i_{Md}^2 + L_{Mq} (i_{Mq} - i_0)^2 + L_B (i_{Bd}^2 + i_{Bq}^2) \right] \\ &\quad + \left[M_d i_{Md} i_{Bd} + M_q (i_{Mq} - i_0) i_{Bq} \right] x_d \\ &\quad - \left[M_d i_{Md} i_{Bq} - M_q (i_{Mq} - i_0) i_{Bd} \right] y_q \end{aligned} \tag{2}$$

The mathematical model of the suspension force in the d-q coordinate system is derived as follows:

$$\begin{aligned} \begin{bmatrix} F_d \\ F_q \end{bmatrix} &= \begin{bmatrix} \partial W_m / \partial x_d \\ \partial W_m / \partial y_q \end{bmatrix} \\ &= \begin{bmatrix} M_d i_{Md} & M_q (i_{Mq} - i_0) \\ M_q (i_{Mq} - i_0) & -M_d i_{Md} \end{bmatrix} \cdot \begin{bmatrix} i_{Bd} \\ i_{Bq} \end{bmatrix} \end{aligned} \tag{3}$$

In addition, the radial suspension force of the rotor also includes the unilateral magnetic pull force proportional to the eccentric displacement of the rotor, so the complete mathematical model of the rotor in the two-phase stationary coordinate system is:

$$\begin{aligned} \begin{bmatrix} F_x \\ F_y \end{bmatrix} &= \sqrt{M_d^2 i_{Md}^2 + M_q^2 (i_{Mq} - i_0)^2} \\ &\quad \cdot \begin{bmatrix} -\cos(2\omega t + \theta) & \sin(2\omega t + \theta) \\ \sin(2\omega t + \theta) & \cos(2\omega t + \theta) \end{bmatrix} \cdot \begin{bmatrix} i_{B\alpha} \\ i_{B\beta} \end{bmatrix} \\ &\quad + \left[k_d i_{Md}^2 + k_q (i_{Mq} - i_0)^2 \right] \cdot \begin{bmatrix} x \\ y \end{bmatrix} \end{aligned} \tag{4}$$

where k_d, k_q are the eccentric displacement constants.

According to the principle of electromechanical conversion, the mathematical model of the electromagnetic torque of PMa-BSynRM is:

$$\begin{aligned} T_e &= \partial W_m / \partial \varphi = P_m \left[(L_{Md} - L_{Mq}) i_{Md} i_{Mq} + \psi_0 i_{Md} \right] \\ &\quad + P_B (M_d x i_0 i_{Bq} + M_q y i_0 i_{Bq}) \\ &\quad \pm \begin{bmatrix} i_{Md} & i_{Mq} \end{bmatrix} \cdot \begin{bmatrix} M_d x_d & -M_q y_q \\ M_d y_q & M_q x_d \end{bmatrix} \cdot \begin{bmatrix} -i_{Bd} \\ i_{Bq} \end{bmatrix} \end{aligned} \tag{5}$$

where P_M, P_B are the pole pair numbers of torque windings and suspension force windings, respectively.

2.3. Analysis of Rotor Vibration Mechanism

The diagram of the rotor eccentricity is shown in Fig. 3. Due to machining errors, there are usually errors in the mass center and geometric center of the rotor, which can lead to unbalance vibration of the rotor during rotation. The presence of rotor eccentricity, where the mass center deviates from the geometric center, induces vibrations that are aggravated by rising motor speeds. The consequent growth in vibration displacement thereby causes a critical deterioration of the suspension performance [17].

In order to realize the vibration compensation of the rotor, it is necessary to analyze the rotor when unbalanced vibration occurs. When the rotor does not have a mass eccentric, according to the rotor dynamics model:

$$\begin{cases} m\ddot{x} + c_x \dot{x} + k_x x = F_x - f_{mx} = (k_c i_x + k_e x) - f_{mx} \\ m\ddot{y} + c_y \dot{y} + k_y y = F_y - f_{my} = (k_c i_y + k_e y) - f_{my} \end{cases} \tag{6}$$

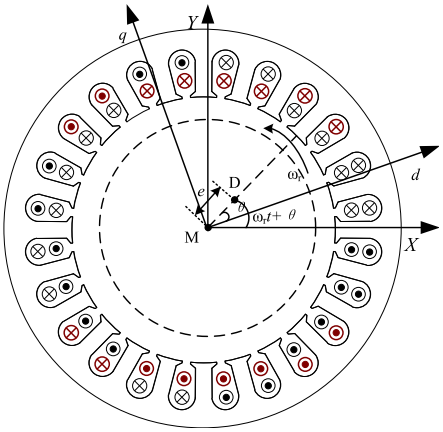

FIGURE 3. Diagram of rotor mass eccentricity.

where c_x and c_y are the coupling coefficients of the rotor; k_x and k_y are the rotor stiffness coefficients; k_c and k_e are the force-current constant and force-displacement constant, respectively; F_x and F_y are the radial suspension forces along the x- and y-directions; f_{mx} and f_{my} are the components of the rotor weight and external loads acting along the x- and y-directions.

When the rotor rotates about the central axis with angular velocity ω_r, a centrifugal force, which varies synchronously with the rotor position, is exerted on the rotor. The components of this force along the x- and y-directions are expressed as follows:

$$\begin{cases} F_{x1} = me\omega_r^2 \cos(\omega_r t + \theta) \\ F_{y1} = me\omega_r^2 \sin(\omega_r t + \theta) \end{cases} \tag{7}$$

where m, ω_r, and θ are the rotor mass, mechanical angular velocity, and initial centroid direction angle, respectively.

The dynamic equations for the eccentric rotor in the x- and y-directions are derived as follows:

$$\begin{cases} m\ddot{x} + c_x\dot{x} + k_x x = F_{x1} + F_x - f_{mx} \\ m\ddot{y} + c_y\dot{y} + k_y y = F_{y1} + F_y - f_{my} \end{cases} \tag{8}$$

From the formula of eccentric force and suspension force:

$$\begin{cases} x = x_0 \cos(wt + \theta - \delta_1) + \Delta x - \frac{f_{mx}}{k_x} \\ y = y_0 \sin(wt + \theta - \delta_2) + \Delta y - \frac{f_{my}}{k_y} \end{cases} \tag{9}$$

where x_0, y_0 are the displacement amplitudes of the rotor eccentric in the x- and y-directions; δ_1, δ_2 are the angles related to the rotor speed, rotor mass, coupling parameters, and stiffness coefficient; Δx, Δy are the uncertain displacement caused by the radial suspension force in the x- and y-directions.

Assuming that PID regulator parameters in x- and y-directions in the controller are the same, the current of the suspension force winding in x- and y-directions can be expressed as;

$$\begin{cases} i_x = -k_p x - k_d\dot{x} - k_i \int_0^t x d\tau \\ i_y = -k_p y - k_d\dot{y} - k_i \int_0^t y d\tau \end{cases} \tag{10}$$

where k_p, k_i, and k_d are PID regulator parameters, respectively. Ignoring the influence of the stiffness and coupling coefficients, solve (8) and (10) to obtain the displacement expression:

$$\begin{cases} \begin{cases} x(t) = A\cos(\omega_r t + \xi) \\ y(t) = A\sin(\omega_r t + \xi) \end{cases} \\ \begin{cases} A = \frac{me\omega_r^3 \cos\theta}{\omega_r[k_c(k_p+k_d) - k_e - 2m\omega_r^2]\cos\xi + k_c k_i \sin\xi} \\ \xi = \theta + \arctan\left[\frac{k_c k_i}{k_c(k_p+k_d)\omega - k_e\omega_r - 2m\omega_r^3}\right] \end{cases} \end{cases} \tag{11}$$

When the rotor mass is eccentric, the rotor produces periodic vibration with the same speed of the frequency. This vibration affects the control and suspension performance of the PMa-BSynRM and even leads to suspension failure. To address this, a novel feed-forward compensation strategy is adopted to actively suppress rotor vibration and improve suspension performance of the PMa-BSynRM.

3. ROTOR UNBALANCE VIBRATION COMPENSATION CONTROL

3.1. LMS Adaptive Filtering Algorithm

The block diagram of the LMS adaptive filtering algorithm is shown in Fig. 4. Here, the primary signal d is the radial displacement signal of the rotor, which contains random displacement components and rotor unbalance displacement components. The reference input signals x_1 and x_2 are sine and cosine signals synchronized with the rotational speed, respectively. The LMS adaptive filter adaptively adjusts the weight coefficients w_1 and w_2 so that the output signal y, after the algorithm converges, matches both the amplitude and phase of the rotor unbalance displacement signal in d. y is the extracted rotor unbalance displacement signal.

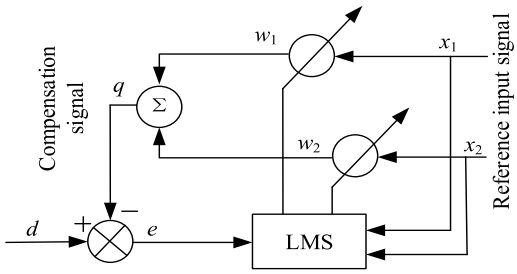

FIGURE 4. Structure block diagram of LMS algorithm.

When the rotor produces displacement in the radial direction, the sensor outputs the rotor radial displacement signal. After conditioning by the displacement interface circuit, the difference is made with the reference equilibrium position to obtain the displacement difference signal, which is denoted as d. The reference equilibrium position signal is 0. The output signal of the sensor contains the vibration signal and rotor actual displacement signal, the signal of which is expressed as follows:

$$d(nT) = d_a(nT) + A\cos(n\omega T + \theta) \tag{12}$$

where T is the sampling period; A is the amplitude of the rotor displacement signal; ω is the rotor angle frequency; θ is the

initial phase angle of the rotor; and d_a is the actual displacement signal of the rotor. Taking the rotor radial x direction as an example, the reference input signal expression is as follows:

$$\begin{cases} x_1(n) = A_1 \sin \omega_r (nT + \phi) \\ x_2(n) = A_2 \cos \omega_r (nT + \phi) \end{cases} \tag{13}$$

where A_1 and A_2 are the amplitude of the rotor displacement signal; ω_r is the rotor angle frequency.

The weight update expression of the traditional LMS algorithm is as follows:

$$\begin{cases} y(n) = w_1(n)x_1(n) + w_2(n)x_2(n) \\ e(n) = d(n) - y(n) \\ w_1(n+1) = w_1(n) + 2\mu(n)e(n)x_1(n) \\ w_2(n+1) = w_2(n) + 2\mu(n)e(n)x_2(n) \end{cases} \tag{14}$$

In the LMS algorithm, the step size μ greatly affects the convergence speed and steady-state accuracy. The smaller the step size is, the higher the steady state accuracy is. While the algorithm convergence speed is slow, the larger the step size is, the faster the convergence is, and the larger the steady state error is. Therefore, the traditional fixed-step LMS algorithm cannot take into account the requirements of convergence speed and steady state accuracy. Moreover, the traditional LMS algorithm will encounter noise interference in practice, which has good convergence performance when dealing with Gaussian noise, but the convergence performance is seriously reduced when facing some non-Gaussian noise with significant pulse properties.

In order to solve the contradiction between the convergence speed and steady-state accuracy of the method, Sigmod function can be used to construct the relationship between the step length of the algorithm and the error signal, so that the step length changes with the certain function relationship of the error signal. The specific function image is shown in Fig. 5. The principle of adjusting the step length by error is: when the initial error is large, the step size should be large to have a fast convergence speed; while when the error is small, keep the small step size. However, the Sig-LMS algorithm affects the steady-state accuracy when the error is small, and it is less robust in the face of pulse interference. Therefore, the BP neural network is used to construct the nonlinear relationship between error and step size shown in Fig. 5.

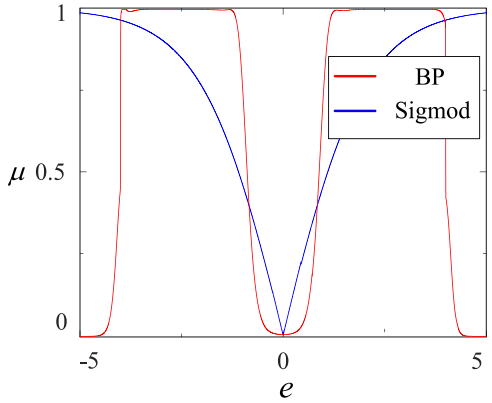

FIGURE 5. Step-size tuning function of LMS algorithm.

As can be seen from Fig. 5, compared with the Sig-LMS algorithm, BP-LMS algorithm adopts a large step size at the beginning of convergence, which becomes smaller as the iteration proceeds, resulting in faster convergence and improved steady-state precision. In addition, with the error over a certain threshold, the step will quickly tend to 0, and the algorithm weight coefficient is not updated, so that the algorithm has a certain resistance to pulse interference.

3.2. BP Neural Network Algorithm

BP neural network is the most widely used artificial neural network so far. The BPNN with two computing layers can fit any nonlinear function with high accuracy, which has the advantages of simple structure, small computational amount, and strong parallelism, and structure is shown in Fig. 6.

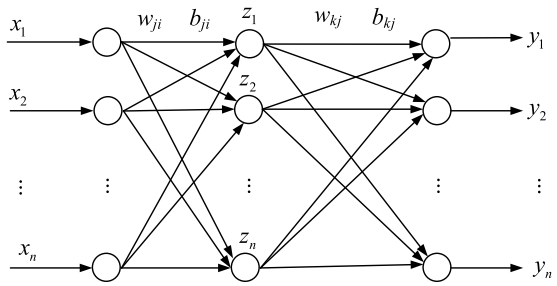

FIGURE 6. BP neural network structure diagram.

The BPNN in each layer is explained as follows:

Input layer: Sample value input vector of hidden layer, each node is written as:

$$O_j^1 = x_j, \quad j = 1, 2, \cdots, 4 \tag{15}$$

where x_j is the input variable of BPNN, and superscripts 1, 2, and 3 indicate the input, implied, and output layers, respectively.

The input vector and output vectors of each node in the hidden layer can be written as:

$$\begin{cases} h_i^2 = \sum_{i=1}^{9} w_{ij} O_j^1 \\ O_i^2 = g_i(h_i^2 - \theta_i) \end{cases} \tag{16}$$

where w_{ij} is the connection weight between j neuron in input layer and i neuron in hidden layer; θ_i is the bias of i neuron in hidden layer; $g_i(x)$ is the activation function of the hidden layer.

$g_i(x)$ adopts the high-priority tanh function with the following expression:

$$g_i(x) = \frac{e^x - e^{-x}}{e^x + e^{-x}} \tag{17}$$

The input vector and output vector of each node in the output layer can be written as:

$$\begin{cases} p_k^3 = \sum_{k=1}^{2} w_{ki} O_i^2 \\ O_k^3 = g_k(p_k^3 - \theta_k) \end{cases} \tag{18}$$

where w_{ki} is the connection weight between the ith neuron in hidden layer and the kth neuron in output layer; θ_k is the bias of the kth neuron in output layer; and $g_k(x)$ is the activation function of the output layer.

$g_k(x)$ is connected to the output of each neuron using a normalized sigmoid function, expressed as follows:

$$g_k(x) = \frac{1}{1+e^{-x}} \tag{19}$$

The fitness function is shown as follows:

$$E_1 = \frac{1}{2}\sum_{i=1}^{N}(y_i - \hat{y}_i)^2 \tag{20}$$

where N is the number of training samples, y_i the actual output, and $\hat{y}_i$ the desired output.

However, the BPNN also has problems such as slow convergence, easy to fall into local minimum and overfitting. The overall performance of the BPNN especially depends on the initial weights and threshold of the network, so how to choose the optimal initial weight and threshold is the key to improve the BPNN.

In this paper, IGA and PSO algorithm are combined to obtain a novel intelligent hybrid algorithm IGAPSO, which has good global optimization ability and fast convergence speed. IGAPSO transforms the selection of initial weights and thresholds in BPNN into an optimization problem of solving the optimal value function. It performs optimization search on this problem and assigns the optimal solution obtained by IGAPSO to the BPNN for offline learning and training. This approach enhances its nonlinear fitting capability while avoiding convergence to local optima.

Particle swarm algorithm (PSO) [18] originates from the feeding behavior of fish flocks and birds. Each particle has four attributes, namely position, experience, speed, fitness; position represents the function independent variable; experience represents the fitness minimum value; speed represents the independent variable change value; fitness is the function value. Assuming that the target is to search in an M-dimensional space with n particles in the group, then x_i is the M-dimensional spatial position vector of the ith particle, and the velocity of the particles is indicated by v_i. The iterative equation for the velocity and position of each particle is:

$$\begin{cases} v_{im}^{k+1} = wv_{im}^k + c_1 r_1 \left(p_{im} - x_{im}^k\right) + c_2 r_2 \left(p_{gm} - x_{im}^k\right) \\ x_{im}^{k+1} = x_{im}^k + v_{im}^{k+1} \end{cases} \tag{21}$$

where k is the number of current iterations; r_1 and r_2 are random numbers between [0, 1], maintaining population diversity; meanwhile c_1 and c_2 are the learning factor, and w is the inertia weight.

If only PSO algorithm is used for optimization, it may lead to premature convergence of the optimization process, causing the algorithm to stagnate in local optima. Therefore, it is essential to integrate GA to form an intelligent hybrid algorithm that enhances global optimization capabilities.

Genetic Algorithm (GA): Genetic algorithm operates by applying selection, crossover, and mutation to chromosomes, where each chromosome represents a potential solution. A fitness function evaluates individual quality, driving the population to evolve toward optimal solutions in a global parallel manner. The crossover and mutation mechanisms inherent in GA effectively mitigate premature convergence issues commonly observed in PSO by maintaining population diversity and enabling exploration of broader solution spaces [19].

In standard GA, direct fitness-based replacement strategy is typically employed, where superior offspring replace parent individuals based on fitness comparisons. While this strategy gradually improves population quality, it may lead to premature clustering around local optima during early iterations. Specifically, when the fitness difference between parents and offspring is minimal, the population can rapidly converge near a local optimum, restricting exploration of the broader search space and hindering the discovery of global optima.

In the replacement process, the Metropolis acceptance criterion is applied: if $P > \text{rand}(0,1)$, the inferior offspring is accepted. This mechanism allows suboptimal solutions to be retained with a probability that decays gradually as iterations increase. By preserving less-fit individuals probabilistically, the algorithm avoids premature convergence, enhances stochastic exploration, and strengthens its capacity to escape local optima, and during early iterations more searches are done.

$$\Delta E = f_s(x_{new}) - f_s(x_{old}),\ P = \begin{cases} 1, & \Delta E < 0 \\ e^{\frac{-\Delta E}{t}}, & \Delta E > 0 \end{cases} \tag{22}$$

Figure 7 is the flowchart of the BPNN optimized by the IGAPSO algorithm. The steps for optimizing the BPNN using the IGAPSO algorithm are as follows:

1) BPNN determination structure generates initial weights and thresholds to the PSO for initializing the population.

2) Using PSO to conduct optimization, the fitness of the algorithm is the error of the BPNN.

3) Incorporate mutation operations, periodic crossover, and Metropolis individual replacement. Output the optimal individual when the maximum iteration count is reached.

4) Assign the global optimal individual identified by IGAPSO to the BPNN for subsequent training.

3.3. Rotor Unbalance Vibration Compensation Based on Variable Step Size LMS Algorithm

The proposed method in this paper employs displacement minimization control strategy. The extracted rotor unbalance signal is transformed into a synchronous rotating coordinate system, where the target value is set to zero. By comparing the transformed signal with the reference, the PID controller generates

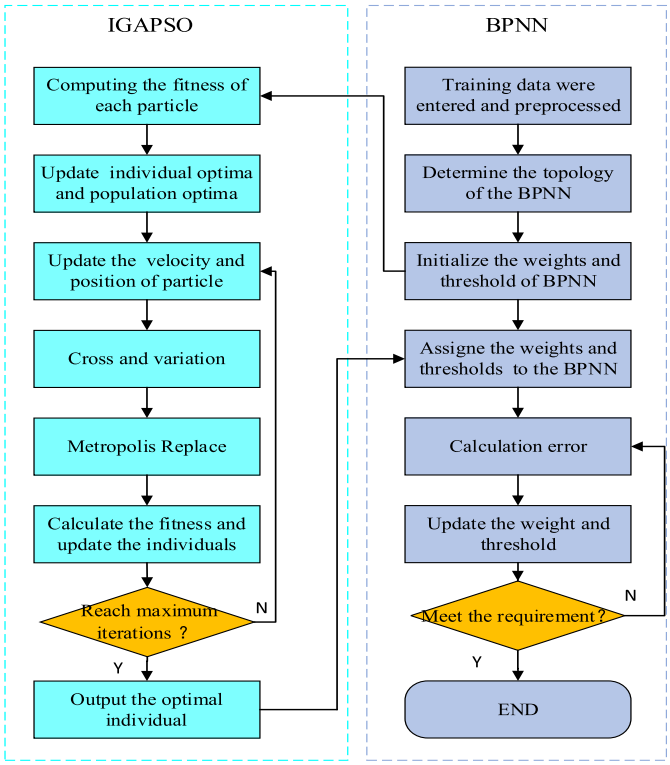

FIGURE 7. Flow chart of the BPNN optimized by the IGAPSO algorithm.

compensation forces in the rotating coordinate system. These forces are then converted to the stationary coordinate system through inverse rotational transformation, achieving active vibration suppression. The detailed control architecture is illustrated in Fig. 8. x' and y' are the rotor unbalance displacement signal extracted from the original displacement signal by BP-LMS adaptive filter, and the two signals are sine and cosine signals with the same frequency as the rotor rotational speed; u and v are the DC signal converted by rotation transformation; F_{xu}^*, F_{yv}^* are the unbalance compensation force signal in the synchronous rotation frame generated by PID; $F_{x\alpha}^*$, $F_{y\beta}^*$ are the unbalance compensation signal in the stationary frame. Fig. 9 is the structural diagram of the BP-LMS algorithm.

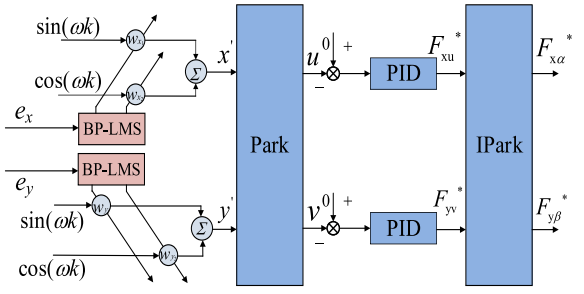

FIGURE 8. Rotor unbalance force suppression model.

Based on inherent characteristics of the rotor unbalance force, the rotor unbalance vibration feedforward compensation controller based on the BP-LMS adaptive filtering algorithm is designed in this paper, which does not need the observer, accurate mathematical model, and unbalance force, and can make the rotor rotate around its geometric center and effectively suppress the unbalance vibration of the rotor.

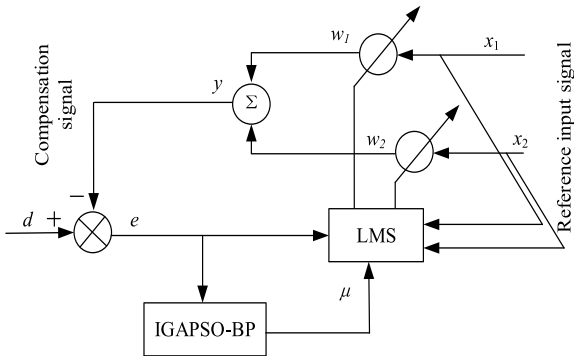

FIGURE 9. Structural diagram of the BP-LMS algorithm.

4. SIMULATION ANALYSIS

4.1. IGAPSO-BP algorithm

This section validates the optimized performance of the IGAPSO for BPNN. The initial weight and threshold of BPNN were optimized using GA, PSO, and IGAPSO in Matlab, and the performances of the GA-BP, PSO-BP, and IGAPSO-BP were compared. The total number of iterations of the IGAPSO algorithm is 150, and crossover operations are performed every 10 generations, with population size 30, inertia weight 0.6, learning factor $c1 = 1.5$, $c2 = 2$, weight range $[-1, 1]$, speed range $[-0.2, 0.2]$, crossover probability 0.7, and variant probability 0.05.

Figure 10 shows the training process of three optimized BPNN models. The PSO-BP converged after 616 times, the error is 0.000104. The GA-BP converged at 151 times, the error is 0.000354, while the IGAPSO-BP converged at 164 times with an error of 0.0000587. Therefore, it can be concluded that IGAPSO-BP combines the three advantages, fast convergence speed, high fitting accuracy, and better training effect.

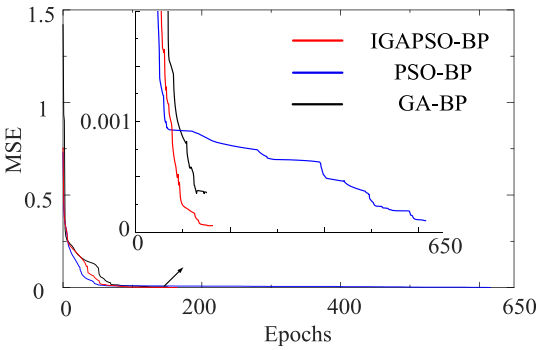

FIGURE 10. Training process of neural network.

4.2. Validation of the Algorithm Extraction Performance

This section validates the performance of the proposed algorithm for extracting the unbalanced signals in the displacement signals. As shown in Fig. 11, a sine wave with frequency of

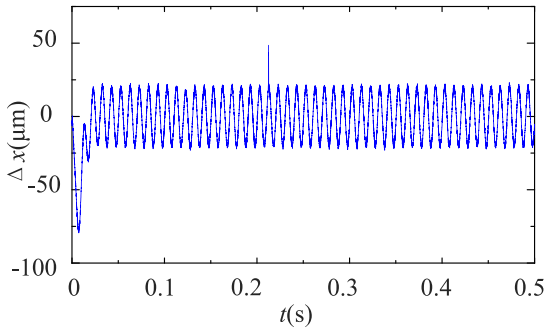

FIGURE 11. Rotor unbalance vibration suppression signal.

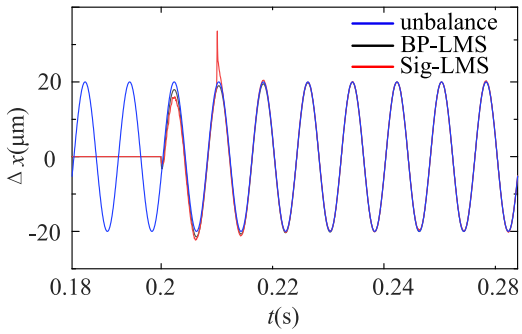

FIGURE 12. The extracts the signals of adaptive filtering algorithm.

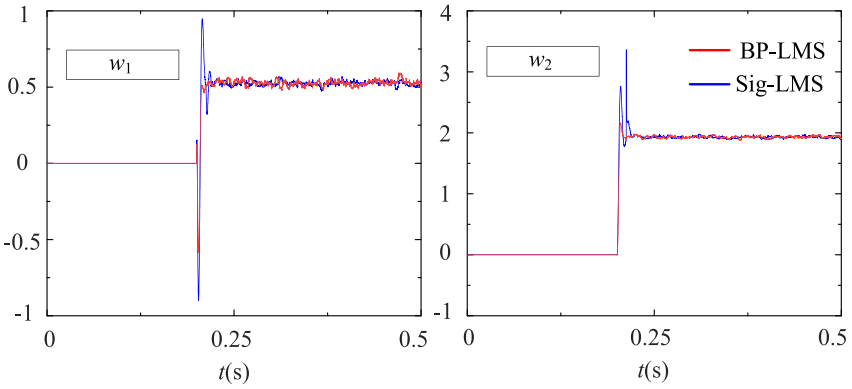

FIGURE 13. The weights of LMS algorithm.

80 Hz and amplitude of 38 μm is added to the rotor displacement waveform in x direction when the PMa-BSynRM runs at 5000 r/min. Gaussian white noise is added, and a pulse signal is given at 0.21 s in the displacement signal, namely at the algorithm input end.

Figure 12 shows the comparison of the unbalance vibration signal extracted by the BP-LMS algorithm and Sig-LMS with the given unbalance signal, accessing the algorithm at 0.2 s. Fig. 13 shows the change of the two weights during the operation of BP-LMS and Sig-LMS. It can be seen that the proposed algorithm is almost not affected by Gaussian white noise and pulse signal, and the convergence speed and accuracy of the algorithm are better than Sig-LMS.

4.3. Simulation of the Vibration Compensation

In order to verify the effectiveness of the proposed rotor unbalance vibration compensation controller based on BP-LMS adaptive filtering algorithm, a two-degree freedom PMa-BSynRM rotor vibration compensation control model was constructed in MATLAB as shown in Fig. 14. Due to the gravity of the rotor, the initial rotor displacement is set to $x = 0$ mm and $y = -0.25$ mm, respectively. The whole control system is composed of two subsystems, torque and suspension. The torque part is controlled by maximum torque per ampere (MTPA), the suspension part controlled by displacement current double closed-loop, and the unbalance displacement compensation controlled by minimum displacement. The error signal obtains F_x and F_y by PID and gets F_{cx}^* and F_{cy}^* by the LMS unbalance vibration compensation module. The unbalance vibration compensation forces F_x^* and F_y^*, obtained by summing F_x, F_y, F_{cx}^*, and F_{cy}^*, are injected into the feedforward channel to achieve rotor unbalance vibration compensation.

In Matlab, the displacement signal containing the rotor vibration signal was simulated by stacking a sine wave at 80 Hz and 50 Hz in the displacement signal at 5000 r/min and 3000 r/min, respectively.

Figures 15 and 16 show the rotor displacement waveform in the x- and y-directions of the rotor at 3000 r/min and 5000 r/min based on BP-LMS and Sig-LMS. As shown in Fig. 15, the rotor runs at 3000 r/min, and the unbalance vibration compensation algorithm is introduced at 0.2 s. Before compensation, the rotor vibration amplitude in the x direction is 29 μm, and the rotor vibration amplitude in the y direction is 31 μm. After compensation, in the x- and y-directions, BP-LMS has faster convergence and higher accuracy than Sig-LMS.

As shown in Fig. 16, with the rotor running at 5000 r/min, before compensation, the rotor displacement waveforms in the x- and y-directions of the rotor are 36 μm and 38 μm, respectively. Unbalance vibration compensation is also introduced at 0.2 s. It can be seen that the rotor displacement amplitudes in x- and y-directions can still converge and stabilize within 0.1 s at 5000 r/min. Compared with Sig-LMS, the initial step size of BP-LMS is larger, the later step size smaller, and the change more stable, so its convergence speed is faster and the steady-state performance better. The simulation results show that the unbalance vibration compensation controller of LMS adaptive

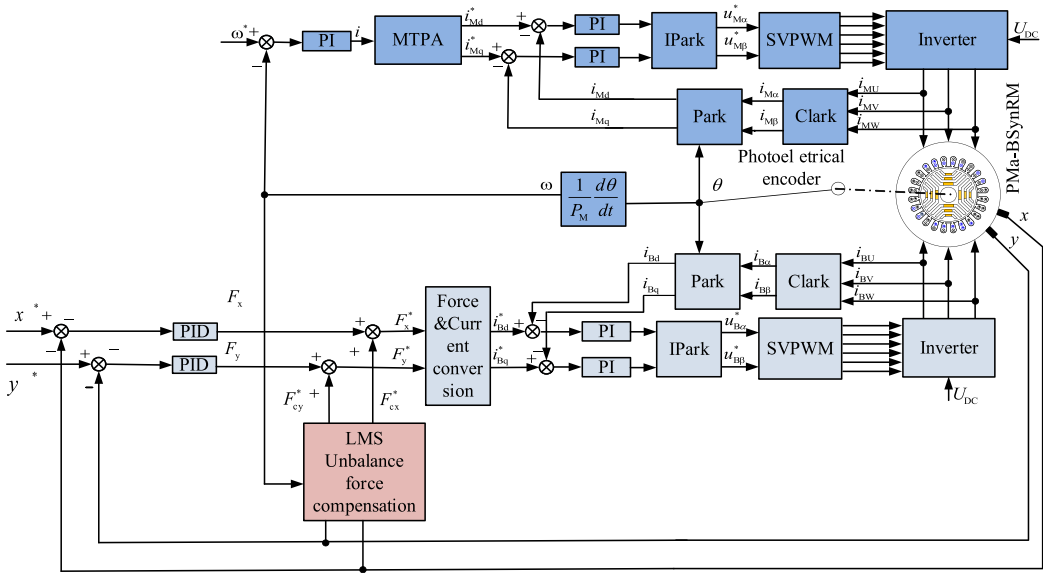

FIGURE 14. Rotor vibration compensation control block diagram of the PMa-BSynRM.

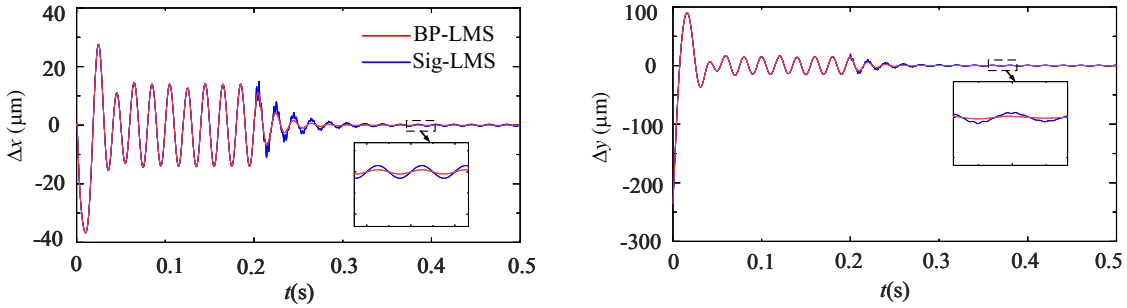

FIGURE 15. Rotor vibration suppression results at 3000 r/min.

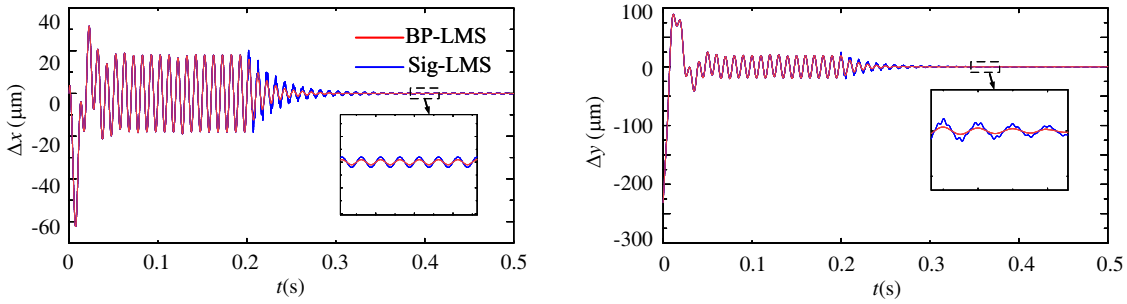

FIGURE 16. Rotor vibration suppression results at 5000 r/min.

filter based on IGAPSO-BPNN has good compensation effect at different speeds and can effectively suppress the unbalance vibration of the rotor.

5. RESULTS AND ANALYSIS OF THE EXPERIMENT

To verify the effectiveness of the proposed control method, comparative experimental studies are conducted in this section. The control objects of the experiment are the PMa-BSynRM with the number of pole pairs of the suspension force winding as 1 and the number of pole pairs of the torque windings as 2.

TABLE 1. Parameters and description of the experimental platform.

Parameters	Values	Parameters	Values
n (r/min)	5 000	U_N (V)	220
δ_0 (mm)	0.25	ψ_0 (Wb)	0.0359
P_N (kW)	1.1	N_M/N_B	72/24
P_M/P_B	2/1	*Volume* (mm^3)	$4 \times (120 \times 71 \times 73)$
m (kg)	1.6	PM material	NdFeB

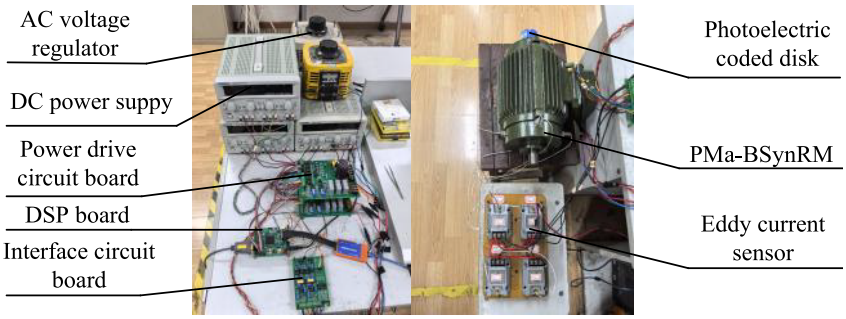

FIGURE 17. The experimental platform of PMa-BSynRM.

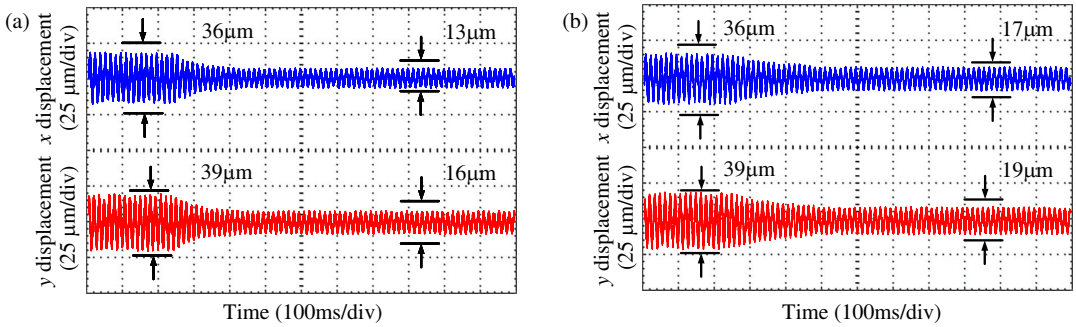

FIGURE 18. Unbalance vibration suppression of rotor displacement. (a) Based on BP-LMS. (b) Based on Sig-LMS.

The PMa-BSynRM is supported by a aligning ball bearing on one end with an auxiliary bearing at the other end which can realize two-degree-of-freedom suspension. The basic parameters of PMa-BSynRM used in the experiment are shown in Table 1. The constructed digital experimental platform is shown in Fig. 17, which mainly includes PMa-BSynRM, digital signal processor (DSP), inverter, PC host, photoelectric encoder disk, and oscilloscope. This paper uses DSP TMS320F28335 as the core digital controller.

5.1. Constant Speed Vibration Suppression Experiment

In this section, the vibration suppression experiment is carried out at constant speed, and the effects of rotor unbalance vibration compensation based on BP-LMS and Sig-LMS adaptive filters are compared.

As shown in Fig. 18, the displacement amplitudes in the x- and y-directions when the rotor runs at 5000 r/min without vibration inhibition are 36 μm and 39 μm, respectively. The rotor amplitude decreases substantially and reaches a steady state after introducing the control algorithm. After introducing the Sig-LMS algorithm, 0.2 s converged, and the amplitudes in the x- and y-directions decrease to 17 μm and 19 μm, respectively, decreased by 55.6% and 51.3% compared to the amplitude before compensation. However, after introducing the BP-LMS algorithm, the displacement response amplitude converges to a steady state within 0.13 s, and the amplitudes of x- and y-directions decrease to 13 μm and 16 μm, respectively, decreased by 63.9% and 58.9% compared with the amplitude before compensation. The experimental results show that BP-LMS algorithm and Sig-LMS algorithm can effectively suppress the rotor amplitude in the x- and y-directions. BP-LMS compared with Sig-LMS has a larger step size and later stage, and considering the influence of noise interference, BP-LMS algorithm converges faster, and the vibration suppression effect is better.

5.2. Acceleration Vibration Suppression Experiment

In this section, the rotor acceleration experiment under the vibration compensation is designed to further verify the unbalance vibration suppression ability based on the BP-LMS adaptive filtering algorithm.

Figure 19 shows the radial displacement waveform in the x- and y-directions when the rotor accelerates from 3000 r/min to 5000 r/min. Without vibration compensation, the rotor perturbation amplitudes are 45 μm in the x-direction and 53 μm in the y-direction with a recovery time of 160 ms. Under the Sig-LMS algorithm, the rotor perturbation amplitudes are 24 μm and 29 μm in the x- and y-directions, with a recovery time of 119 ms, respectively. However, under the BP-LMS, rotor perturbation amplitudes are 20 μm in the x-direction and 26 μm in the y-direction, with a recovery time of 102 ms. According to the experimental results, the proposed vibration compensation method can still realize the stable suspension of the rotor when the rotor speed changes and has a better vibration suppression effect.

5.3. Disturbance Experiment

To validate the anti-interference and robustness of the proposed algorithm, disturbance experiments of the rotor are carried out.

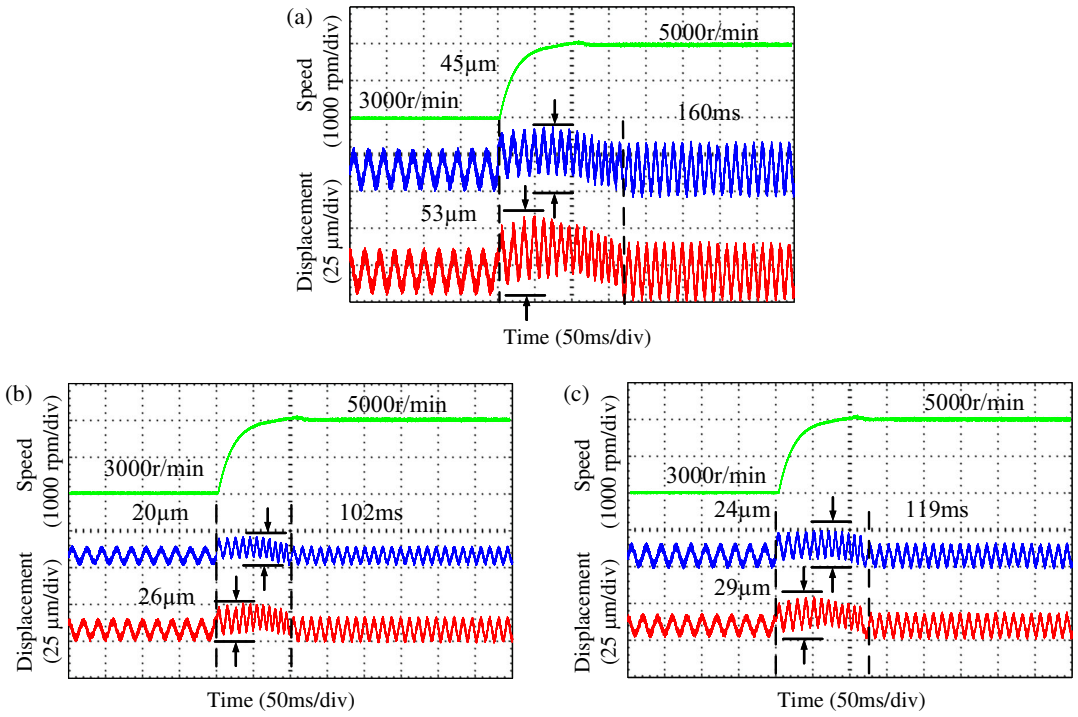

FIGURE 19. Displacement waveform of the rotor accelerating experiment. (a) Without compensation. (b) Based on BP-LMS. (c) Based on Sig-LMS.

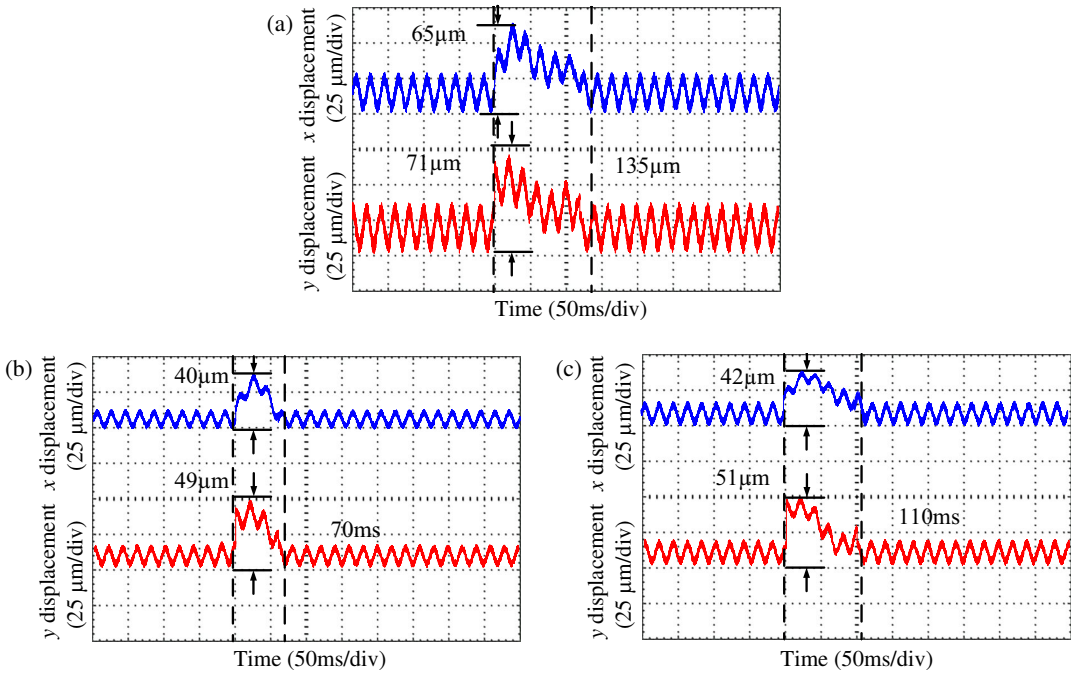

FIGURE 20. Displacement waveform of disturbing force applied in the y direction. (a) Without compensation. (b) Based on BP-LMS. (c) Based on Sig-LMS.

When the rotor runs stably at 3000 r/min, a 40 N interference force is added to the rotor in the y-direction. As shown in Fig. 20, the vibration amplitudes of the rotor in the x- and y-directions are 65 μm and 71 μm, respectively, with an adjustment time of 135 ms. The vibration amplitudes based on the Sig-LMS algorithm are 42 μm and 51 μm in the x- and y-directions, respectively, with a adjustment time of 110 ms. However, the vibration amplitudes based on BP-LMS proposed in this paper can still effectively suppress the unbalance vibration of the rotor under the action of interference force, and the vibration amplitudes in x- and y-directions are 40 μm and 49 μm, respectively, and the adjustment time is 70 ms. The above experimental results show that the unbalance controller based on proposed BP-LMS has better anti-interference and ro-

bustness, with smaller perturbation and faster recovery, when the interference force occurs in the y-direction.

6. CONCLUSION

In order to solve rotor unbalance vibration in PMa-BSynRM, an unbalance feedforward compensation control method based on LMS adaptive filtering algorithm optimized by BPNN is proposed, and the following conclusions are drawn through simulation and experiments.

1) The BP-LMS algorithm uses BPNN to adjust the step size of the LMS. Compared with Sig-LMS, it has faster convergence, higher accuracy and anti-interference ability.

2) Aiming at the slow convergence rate of BPNN and the easy to fall into local minimum, the PSO and IGA are combined to optimize the initial weights and thresholds of BPNN, accelerating the convergence speed and improving fitting accuracy.

3) The proposed algorithm can effectively alleviate the unbalance vibration and show superior vibration suppression performance under the constant speed operation. Moreover, rotor acceleration and perturbation experiments show better anti-interference and robustness.

ACKNOWLEDGEMENT

This project was sponsored in part by National Natural Science Foundation of China (62273168).

REFERENCES

[1] Mao, B. and H. Zhu, "Unbalance vibration suppression control of PMa-BSynRM based on total least square adaptive filtering algorithm," *IEEE Journal of Emerging and Selected Topics in Power Electronics*, Vol. 11, No. 6, 5798–5808, Dec. 2023.

[2] Gao, Y., D. Jiang, H. Zhu, B. Mao, and Y. Liu, "Design optimization of asymmetric permanent magnet assisted bearingless synchronous reluctance motor," *IEEE Transactions on Energy Conversion*, Vol. 40, No. 2, 1644–1654, Jun. 2025.

[3] Setiawan, J. D., R. Mukherjee, and E. H. Maslen, "Synchronous disturbance compensation in active magnetic bearings using bias current excitation," in *2001 IEEE/ASME International Conference on Advanced Intelligent Mechatronics, Proceedings (Cat. No. 01TH8556)*, Vol. 2, 707–712, Como, Italy, Jul. 2001.

[4] Shafai, B., S. Beale, P. LaRocca, and E. Cusson, "Magnetic bearing control systems and adaptive forced balancing," *IEEE Control Systems Magazine*, Vol. 14, No. 2, 4–13, Apr. 1994.

[5] Peng, C., M. Zhu, K. Wang, Y. Ren, and Z. Deng, "A two-stage synchronous vibration control for magnetically suspended rotor system in the full speed range," *IEEE Transactions on Industrial Electronics*, Vol. 67, No. 1, 480–489, Jan. 2020.

[6] Herzog, R., P. Buhler, C. Gahler, and R. Larsonneur, "Unbalance compensation using generalized notch filters in the multivariable feedback of magnetic bearings," *IEEE Transactions on Control Systems Technology*, Vol. 4, No. 5, 580–586, Sep. 1996.

[7] Schuhmann, T., W. Hofmann, and R. Werner, "Improving operational performance of active magnetic bearings using Kalman filter and state feedback control," *IEEE Transactions on Industrial Electronics*, Vol. 59, No. 2, 821–829, Feb. 2012.

[8] Gong, L. and C. Zhu, "Synchronous vibration control for magnetically suspended rotor system using a variable angle compensation algorithm," *IEEE Transactions on Industrial Electronics*, Vol. 68, No. 8, 6547–6559, Aug. 2021.

[9] Chen, K.-Y., P.-C. Tung, M.-T. Tsai, and Y.-H. Fan, "A self-tuning fuzzy PID-type controller design for unbalance compensation in an active magnetic bearing," *Expert Systems with Applications*, Vol. 36, No. 4, 8560–8570, May 2009.

[10] Mao, C. and C. Zhu, "Unbalance compensation for active magnetic bearing rotor system using a variable step size real-time iterative seeking algorithm," *IEEE Transactions on Industrial Electronics*, Vol. 65, No. 5, 4177–4186, May 2018.

[11] Jiang, K., C. Zhu, and L. Chen, "Unbalance compensation by recursive seeking unbalance mass position in active magnetic bearing-rotor system," *IEEE Transactions on Industrial Electronics*, Vol. 62, No. 9, 5655–5664, Sep. 2015.

[12] Tiwari, R. and A. Chougale, "Identification of bearing dynamic parameters and unbalance states in a flexible rotor system fully levitated on active magnetic bearings," *Mechatronics*, Vol. 24, No. 3, 274–286, Apr. 2014.

[13] Mao, C. and C. Zhu, "Vibration control for active magnetic bearing rotor system of high-speed flywheel energy storage system in a wide range of speed," in *2016 IEEE Vehicle Power and Propulsion Conference (VPPC)*, 1–6, Hangzhou, China, Oct. 2016.

[14] Shi, J. and H. Zhu, "Control study for compensating rotor vibration of four-DOF six-pole hybrid magnetic bearings based on variable step size LMS algorithm," *IEEE Journal of Emerging and Selected Topics in Power Electronics*, Vol. 11, No. 2, 1616–1626, Apr. 2023.

[15] Kumar, K., R. Pandey, S. S. Bora, and N. V. George, "A robust family of algorithms for adaptive filtering based on the arctangent framework," *IEEE Transactions on Circuits and Systems II: Express Briefs*, Vol. 69, No. 3, 1967–1971, Mar. 2022.

[16] Zhu, H. and Y. Shi, "Displacement self-sensing control of permanent magnet assisted bearingless synchronous reluctance motor based on least square support vector machine optimized by improved NSGA-II," *IEEE Transactions on Industrial Electronics*, Vol. 71, No. 2, 1201–1211, Feb. 2024.

[17] Zhu, H., Z. Yang, X. Sun, D. Wang, and X. Chen, "Rotor vibration control of a bearingless induction motor based on unbalanced force feed-forward compensation and current compensation," *IEEE Access*, Vol. 8, 12 988–12 998, 2020.

[18] Memon, M. A., M. D. Siddique, S. Mekhilef, and M. Mubin, "Asynchronous particle swarm optimization-genetic algorithm (APSO-GA) based selective harmonic elimination in a cascaded H-bridge multilevel inverter," *IEEE Transactions on Industrial Electronics*, Vol. 69, No. 2, 1477–1487, Feb. 2022.

[19] Xu, B., H. Zhu, and X. Wang, "Decoupling control of outer rotor coreless bearingless permanent magnet synchronous motor based on least squares support vector machine generalized inverse optimized by improved genetic algorithm," *IEEE Transactions on Industrial Electronics*, Vol. 69, No. 12, 12 182–12 190, Dec. 2022.